MTLA 39 (2025) 102343

Contents lists available at ScienceDirect

Materialia

journal homepage: www.elsevier.com/locate/mtla

Full length article

# Impact of friction stir welding-like heat cycles on precipitates in AA7050 analysed by SAXS and numerical modelling

Susanne Henninger [a,*], Rupesh Chafle [b], Emad Maawad [a], Benjamin Klusemann [b,c], Martin Müller [a], Peter Staron [a]

[a] Helmholtz-Zentrum Hereon, Institute for Materials Physics, Max–Planck-Straße 1, 21502 Geesthacht, Germany
[b] Helmholtz-Zentrum Hereon, Institute of Material and Process Design, Max–Planck-Straße 1, 21502 Geesthacht, Germany
[c] Leuphana University Lüneburg, Institute for Production Technology and Systems, Universitätsallee 1, 21335, Lüneburg, Germany

ARTICLE INFO

Dataset link: https://doi.org/10.5281/zenodo.14749904

*Keywords:*
Aluminum alloy
Precipitation
Friction stir welding
Modelling
Pandat

ABSTRACT

Precipitation kinetics in AA7050 during heat cycles as they occur in friction stir welding (FSW) were studied via small-angle X-ray scattering (SAXS), X-ray diffraction (XRD) and numerical modelling using the PanPrecipitation software. Reversion experiments were conducted for the calibration of the used model and the reversion stages of dissolution, growth and coarsening of precipitates are successfully modelled. Additionally, reversion experiments on an AA7108 alloy from literature data were modelled, affirming that other AA7xxx alloys can be described with the developed model as well. The model was used to predict precipitation kinetics in AA7050-T7451 during heat cycles typically occurring in FSW, enabling the prediction of the evolution of volume fraction and precipitate size distribution of $\eta$-precipitates at elevated temperatures, matching experimental results. For instance, with increasing temperature, stronger coarsening as well as lower final volume fractions are expected. Finally, the influence of maximum temperature and welding speed on the precipitate size distribution was studied, providing guidelines for temperature-driven process design.

## 1. Introduction

Aluminum alloys of the 7xxx series are widely used in lightweight applications such as aircraft wings or large-volume fuel tanks in aerospace due to their high strength and toughness [1–3]. Their mechanical properties mainly depend on hardening precipitates, which are formed through artificial aging. The typical precipitation sequence in these alloys is supersaturated solid solution (SSSS) → GP zones → $\eta'$ → $\eta$ ($MgZn_2$) [2,4]. Typically, a two-step aging process is used to adjust the precipitate sizes and volume fractions. The maximum hardness and strength, mainly attributed to the presence of $\eta'$-precipitates, are achieved in the peak-aged T6 temper [2,5]. However, the T6 state has poor corrosion resistance; therefore, AA7xxx alloys are often used in an over-aged T7 temper, showing a better corrosion resistance [6]. In overaged states, mainly $\eta$-phase precipitates with the equilibrium composition of $MgZn_2$ are present [6,7].

For application purposes, different parts are required to be joined. High-strength aluminum alloys are usually difficult to weld due to problems such as porosity, hot cracks or the poor resultant microstructure within the fusion zone [3]. In 1991, The Welding Institute (TWI Ltd.) invented a solid-state joining technique called friction stir welding (FSW) that bypasses issues related to fusion-based welding processes since the process operates below the melting point and enables welding of AA7xxx alloys [3]. During FSW, a rotating non-consumable tool plunges into two overlapping or adjacent sheets. The frictional heat and shearing between the material and the tool lead to plastic deformation and the material flows around the tool. The tool traverses and leaves a consolidated joint behind it [3,8]. Although the process operates below the melting point, a complete transformation of the microstructure is observed. The high heating and cooling rates as well as the severe plastic deformation during the process result in different microstructural zones. The stir zone (SZ) experiences the highest plastic deformation and temperatures through the stirring and a completely new microstructure emerges. Precipitates might get dissolved and dynamic recrystallization leads to small grain size within the SZ. In the thermo-mechanically affected zone (TMAZ) the material is still affected by the elevated temperatures and deformed, which leads to a partly recrystallized, partly recovered microstructure [8]. In the heat-affected zone (HAZ), the material is influenced by temperature, but undergoes no plastic deformation [3,8]. The hardness minimum in FSW joints usually lies at the border of HAZ/TMAZ due to precipitation dissolution and coarsening [8], representing therefore an area of significant interest to comprehend the underlying mechanisms.

* Corresponding author.
*E-mail address:* susanne.henninger@hereon.de (S. Henninger).

https://doi.org/10.1016/j.mtla.2025.102343
Received 1 October 2024; Accepted 16 January 2025
Available online 22 January 2025

For a deeper understanding of the occurring phase transformations, dissolution and growth of hardening precipitates in the AA7xxx alloys, it is usually not sufficient to study them ex-situ, i.e. before and after welding. In-situ experiments at synchrotron beamlines offer the possibility and sufficient time resolution for analysing these mechanisms during the process. With small-angle X-ray scattering (SAXS), the size distribution of precipitates can be determined. In-situ FSW experiments were carried out by dos Santos et al. [8], which require a specialized machine, large time effort as well as access to beamlines. In contrast, studies on the influence of temperature cycles on the microstructure can be carried out in a quenching dilatometer [9], requiring significantly less experimental effort. Temperature cycles as they occur, e.g., in the HAZ can be simulated and the size distribution of precipitates can be monitored in-situ with high time resolution, allowing an in-depth understanding of the underlying mechanism related to the thermal loading during the FSW process. Through such in-situ heat treatments, numerical precipitation models can be precisely calibrated.

For the full analysis and interpretation of such in-situ results, numerical modelling of the precipitation kinetics is required. For instance, Pandat [10] and ThermoCalc [11] are leading commercial software packages for modelling in materials science, which are based on the Calphad method for thermodynamic analysis, allowing the modelling of precipitation kinetics in multi-component alloys. For instance, Pandat has been used to model precipitation kinetics of $\gamma'$ precipitates in a Ni-14 at.% Al alloy during isothermal annealing at 550 °C [12]. It has also been deployed for modelling precipitation kinetics in AA6xxx alloys [13], where precipitates with a composition of $Mg_5Si_6$ were assumed for AA6082 and the Kampmann Wagner numerical (KWN) model [14] was used. The model predicted hardening and softening during artificial aging followed by reheating in good agreement with experimental results [13]. This shows the successful modelling of precipitation kinetics in Al alloys using Pandat. However, to the best of the authors knowledge, no work of modelling precipitation kinetics during welding experiments in AA7xxx alloys with Pandat has been published so far. In the present work, Pandat with its aluminum database was used to describe precipitation kinetics in an AA7050 alloy.

A precipitation kinetics model requires input parameters that depend on the specific alloy and precipitate under investigation. Pandat needs the interfacial energy between precipitate and matrix and a kinetic parameter, influencing diffusion, as input parameters. In order to optimize these two parameters, experiments need to be carried out. Reversion experiments (quick heating to a temperature and holding it) have been proven as very useful for this purpose as they give access to the relevant parameters [15,16]. Therefore, in this work we performed in-situ reversion experiments in a dilatometer at different temperatures on AA7050-T7451. To confirm that the calibrated model can also describe similar alloys, we modelled reversion experiments on AA7108.50 based on literature data.

The calibrated model was used for analysing the in-situ SAXS data obtained from simulated temperature cycles typically occurring in the HAZ during FSW processes of AA7050. Finally, the model was used to predict the influence of different welding speeds and different maximum temperatures on the final precipitate volume fraction and mean radius of the precipitate size distribution in AA7050, providing guidelines for the FSW process.

## 2. Experimental

### 2.1. Material

A commercial AA7050 alloy in the over-aged T7451 temper was used in the dilatometer experiments. Cuboidal samples with a size of 10 mm × 5 mm × 6 mm were machined from the delivered sheets. The chemical composition of the material was measured by ESA Eidam & Seiferling Analytik GmbH and the results can be found in Table 1.

**Table 1**
Composition of the used AA7050 alloy in wt.%, measured by ESA Eidam & Seiferling Analytik GmbH.

| Alloy | Al | Zn | Cu | Mg | Fe | Zr | Ti | Si | Mn |
|---|---|---|---|---|---|---|---|---|---|
| AA7050 | bal. | 6.41 | 2.22 | 2.03 | 0.089 | 0.073 | 0.048 | 0.042 | 0.007 |

### 2.2. Heat treatments

The AA7050-T7451 samples were heated via induction using the modified dilatometer DIL 805A/D (TA Instruments) [9]. The temperature was measured using S-type thermocouples, which were spot-welded onto the surface of the aluminum samples, in the centre of the sample, close to the measured volume. A beam size of 0.21 mm × 0.23 mm was used and a sample thickness of 6 mm was irradiated, leading to a measured volume of 0.29 $mm^3$. The heat treatments were conducted in-situ under argon atmosphere, while SAXS and XRD were measured in transmission mode, see details in the following section.

For the reversion experiments, the samples were heated at a rate of 100 K/s to the reversion temperatures of 200, 230, 260 and 290 °C. Subsequently, the temperature was kept constant for up to 2700 s. An exemplary set of small-angle scattering curves is shown in Fig. 1(a) for the reversion experiment at 290 °C. The SAXS intensity has decreased significantly after 25.4 s, when the maximum temperature is reached, corresponding to a reduction in precipitate volume fraction due to dissolution of precipitates. The corresponding size distributions, Fig. 1(b), show that after some time at the reversion temperature the volume fraction increases again and the precipitates grow, shifting the size distribution to larger radii. The final volume fraction after long aging depends on the reversion temperature. For the FSW heating cycles, generic time–temperature curves with maximum temperatures of 230, 260 and 310 °C were used that are based on thermocouple measurements in a FSW experiment of AA7449 carried out by dos Santos et al. [8], where they used a welding speed of 5 mm/s and a rotational speed of 1300 RPM. The applied time–temperature curves correspond to a distance between 8–13 mm lateral to the welding tool. Kamp et al. [17] also studied FSW welding cycles and obtained similar time–temperature curves via thermal modelling of the FSW process.

### 2.3. Synchrotron experiments

Simultaneous in-situ SAXS and XRD measurements were performed during various beam times at the high-energy materials science beamline P07 at PETRA III, which is run by Helmholtz-Zentrum Hereon at Deutsches Elektronen-Synchroron (DESY), Germany [18]. A photon energy of 73 keV, which corresponds to a wavelength of 0.170 Å, was used for all experiments.

The measurements were conducted using PerkinElmer (PE) XRD 1621 flat panel detectors and a Varex XRD 4343 detector. The PE detector has a pixel size of 200 µm × 200 µm and a total number of 2048 × 2048 pixels. The Varex detector has a pixel size of 150 µm × 150 µm and a total number of 2880 × 2880 pixels. A tungsten beamstop with a diameter of 200 µm was used to protect the detector from the primary beam. Silver behenate was used as calibrant for the SAXS detector distance. A distance of 10.6 m between the sample and the SAXS detector was determined. Beam stop and dead pixels were masked before the integration, so that they do not affect the results. A transmission of 62 % was measured for the 6 mm thick AA7050 samples. During the first 180 s of the reversion experiments, contiguous detector images were recorded with an exposure time of 0.4 s. After 180 s, the exposure time was 5 s and an image was taken every 13 s until the end of the experiments. During the welding temperature cycles, contiguous detector images were taken with an exposure time of 0.45 s. After the subtraction of the background, the scattering signal was azimuthally integrated using the Nika-software [19]. A q-range of 0.007–0.4 $A^{-1}$ was analysed. $LaB_6$ was used as calibrant for the XRD

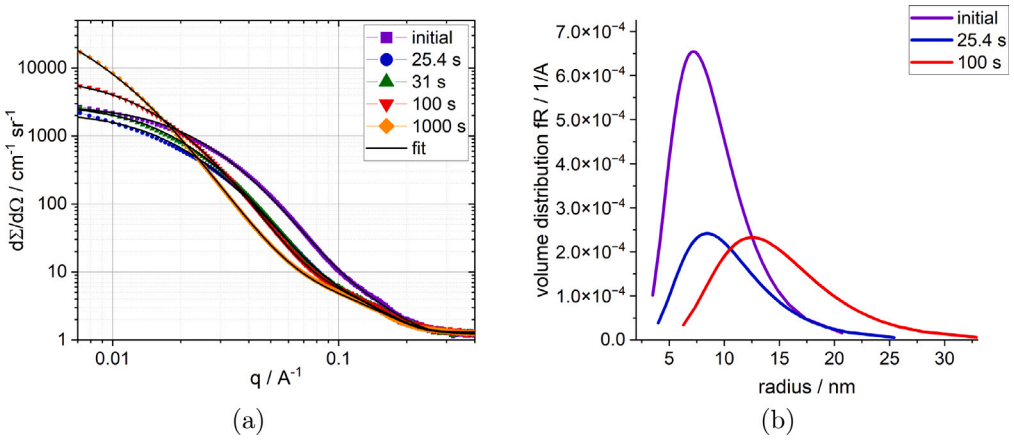


**Fig. 1.** Reversion experiment of AA7050-T7451 at 290 °C: (a) fitted SAXS curves, where the fit is based on the corresponding precipitate size distribution (b).

signal and the sample-detector distance was 3.1 m. Since SAXS and XRD signals were recorded simultaneously, only a part of the diffraction rings could be observed and a sector of the rings with a width of 50° was azimuthally integrated.

The Irena software [20] was used for fitting the SAXS scattering curves. Since the starting state of the alloy was T7451, the expected main phase is $\eta$, with smaller amounts of $\eta'$-phase, which is neglected in this work. Glassy carbon was used for calibration to absolute values of the scattering cross-section. The equilibrium composition of $MgZn_2$ was assumed for the precipitates, having a density of 5.09 g/cm$^3$ [21], which leads to a scattering contrast $(\Delta\rho)^2$ of 3.25 $\cdot 10^{20}$ cm$^{-4}$ between precipitates and Al-matrix. The compositions of both precipitates and matrix are assumed to be constant during the experiments and thus, the scattering contrast was not varied. Alloy composition, heat treatments and solute diffusivity have an impact on the composition of precipitates in Al-Mg-Zn-Cu alloys. Thus, in non-equilibrium conditions, Cu and Al can be present in the precipitates as well. Both Al and Cu can replace Zn on its lattice sites, while Mg is fixed on the other sublattice [22]. However, this is not expected to change the basic precipitation kinetics. Since we do not know the exact composition of the precipitates during these heat treatments, constant equilibrium composition ($MgZn_2$) is assumed as the alloy is used in an over-aged T7451 state.

In the Pandat model, AA7050 was treated as a ternary Al-6.41 Zn-2.03 Mg (in wt.%) alloy and the $\eta$ precipitates were assumed to have the equilibrium composition $MgZn_2$ (cf. Section 3). Based on the thermodynamic calculations, a volume fraction of 4.5% was obtained for the base material. The volume fraction derived from the SAXS scattering curves, using the calibration with glassy carbon, was lower (3.7%), which is attributed to non-stoichiometric precipitate composition and resulting difference in scattering contrast. Hence, the scattering curves were calibrated to a volume fraction of the base material of 4.5%. A common lognormal size distribution was used for the precipitates, and a spheroidal precipitate shape was assumed with an aspect ratio of 0.4 based on literature results [23]. All experiments were fitted using one specific volumetric size distribution, which is specified in the following section. An additional background was separately accounted for, most likely coming from the experimental set-up and depending on temperature.

## 3. Modelling precipitation kinetics with Pandat

In the present study, the commercial Pandat software by CompuTherm LLC is used for modelling the thermodynamics and precipitation kinetics in aluminum alloys [12]. PanEngine calculates the stable phase equilibria for multi-component systems by minimization of the Gibbs energy functions. Based on the embedded thermodynamic, kinetic and thermophysical databases, the PanPrecipitation module allows the calculation of precipitation kinetics such as temporal evolution of volume fraction, number density and average particle size during heat treatments. For the description of kinetics the KWN model is chosen [12,14]. This model categorizes the continuous size distribution into a large number of discrete particle size classes and calculates the size evolution at every time step. The matrix composition is recalculated ensuring mass conservation at each time step, and particle size distributions and volume fractions are updated. Classical nucleation theory and diffusion-controlled growth theory are used to describe nucleation, dissolution, growth and coarsening of precipitates. During all simulation steps, PanPrecipitation is coupled with PanEngine, which provides diffusivity, driving force and thermodynamics. Details on the models and equations used in Pandat can be found in [12].

PanEngine with the PanAluminum database was used for the calculation of thermodynamic equilibrium at room temperature. The used AA7050 alloy was treated as a ternary Al alloy with the composition Al-6.41 Zn-2.03 Mg (in wt.%). It is known that Cu also influences precipitation kinetics in AA7xxx alloys. For instance, in the equilibrium condition, $\eta$-phase has the stochiometric composition $MgZn_2$, but in non-equilibrium conditions, Cu can be enriched in the $\eta$-precipitates [22]. According to Kamp et al. [17], who developed a KWN model for the description of AA7449, the model complexity is highly reduced by neglecting variations in precipitate chemistry, but modelling results are not greatly influenced. Therefore, treating AA7050 as a ternary alloy is assumed to be a reasonable approximation. Since the alloy was used in an overaged T7451 condition, it is assumed that the alloy is close to equilibrium. Only the C14-Laves phase, which describes the $\eta$-phase $MgZn_2$, is regarded in the Al-matrix. As mentioned already above, Pandat calculates an equilibrium volume fraction of 4.5% $\eta$-phase for this alloy. A lognormal size distribution with a standard deviation of 0.4, with a volume fraction of 4.5% and a volumetric mean radius of 8.04 nm with an aspect ratio of 0.4 was defined as starting size distribution in the current model. The KWN model with 100 size classes was used.

PanPrecipitation calculates the mean radius as the average of the particle number density distribution. In contrast, in the SAXS analysis the mean radius is defined as the average of the particle volume distribution, where ellipsoidal shapes of precipitates were assumed. However, in Pandat only spherical and cylindrical particle shapes with different aspect ratios can be selected for precipitates, but no ellipsoidal shapes. Therefore, the shape of all particles was considered spherical for Pandat calculations. During post-processing, a conversion to the volumetric mean radii of ellipsoidal particles with an aspect ratio of 0.4 to match it with the experiments was performed. Consequently, the mean radius is defined as the mean semi-major axis of the spheroids. Additionally, the influence of the ellipsoidal shape with aspect ratio 0.4 on the precipitation kinetics is expected to be very small. A molar volume of 1.015 $\cdot 10^{-5}$ m$^3$/mol for the $\eta$-precipitates [24] and 1.0425

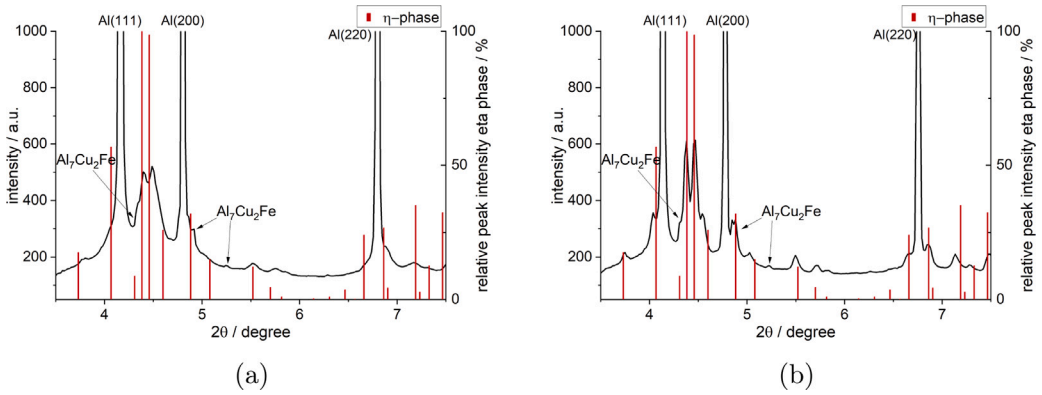


**Fig. 2.** XRD results of the reversion experiment: (a) AA7050-T7451 base material at room temperature, (b) AA7050-T7451 after 1800 s at 260 °C. The crystal structure of The Materials Project mp-1124 [26,27] was assumed for $\eta$. Powder Cell [28] was used for the calculation of the resulting X-ray pattern. The red bars indicate the positions and intensities of $\eta$-phase peaks. $Al_7Cu_2Fe$ is present, but is not dissolved in the investigated temperature range.

$\cdot 10^{-5}$ $m^3$/mol for the aluminum matrix [25] are assumed. The precipitate phase is stochiometric and therefore, assumed to have constant composition throughout the study. The contribution from elastic effects is neglected for simplicity.

Reversion experiments were conducted for simultaneous calibration of interfacial energy and the kinetic parameter factor of the model. In a reversion experiment, only dissolution and growth of precipitates occur; thus, nucleation can be neglected [16]. Parameters that are usually calibrated with these experiments are solubility, interfacial energy and diffusion constant. The solubility, which influences the equilibrium volume fraction, is calculated by Pandat using the thermodynamic database and, thus, is not a free parameter in the model. Through a change in interfacial energy, the volume fraction minima during the heating step can be adapted. The diffusion constant changes the kinetics during the reversion and therefore, leads to a shift on the time axis. Additionally, it impacts the growth and coarsening of precipitates [16]. In this work, interfacial energy and kinetic parameter factor, which is a prefactor to the diffusion constant, are calibrated on the SAXS reversions experiments. An interfacial energy of 0.12 J/$m^2$ was obtained through fitting, which is close to literature data for $\eta$ of 0.2 J/$m^2$ given by Kamp et al. [17] for AA7449. The kinetic parameter factor was fitted as well and it was set to a value of 3. These values for the interfacial energy and kinetic parameter factor were kept constant during all simulations.

The calibrated model was used to validate literature reversion data on the aluminum alloy AA7108.50 with the composition Al-5 Zn-0.8 Mg-0.16 Zr (in wt.%) in T7 condition [15]. This alloy was also modelled as a ternary alloy, i.e. Al-5 Zn-0.8 Mg (in wt.%). Then the model was used to study the influence of typical FSW temperature cycles on AA7050. Finally, the model was used for predicting the influence of maximum welding temperature and different welding speeds on volume fraction and mean radius on $\eta$-precipitates.

## 4. Results and discussion

### 4.1. X-ray diffraction

From the diffraction pattern, it can be seen that precipitates of the $\eta$-phase are already present in the AA7050-T7451 base material, Fig. 2(a). The $\eta$-phase is a Laves phase with the composition $MgZn_2$ and a crystal structure with the space group $P6_3/mmc$ and lattice parameters of a = 0.5221 nm and c = 0.8567 nm [7,29]. The calculated relative intensities of the $\eta$-phase are based on the crystal structure of the Materials Project mp-1124 [26,27]. The software Powder Cell was used for the simulation of resulting X-ray powder patterns [28].

The diffraction patterns also indicate the presence of peaks that belong to the intermetallic $Al_7Cu_2Fe$-phase, see Fig. 2(a). $Al_7Cu_2Fe$ has a tetragonal crystal structure with the space group P4/mnc and cell parameters a = 0.633 nm, c = 1.481 nm [30]. The $Al_7Cu_2Fe$ peak positions indicated in Fig. 2 are based on the crystal structure given by the Materials Project mp-4689 [27,31]. Li and Starink [1] found $Al_7Cu_2Fe$ particles with a size of 15 μm clustered in bands. Robson and Prangnell [32] reported intermetallic particles at grain boundaries in an AA7050 alloy. These particles are stable at higher temperatures and do not dissolve at the temperatures relevant for this work. Due to their large size it is not possible to detect them in the SAXS signal of the present experiment as the investigated Q-range does not cover small enough values.

Starting from a quenched state, the metastable $\eta'$ phase forms first from solid solution. Controversies still exist about the crystal structure of $\eta'$-precipitates, so several structural models have been suggested. It is known that the precipitates have a hexagonal, semi-coherent crystal structure. However, it is difficult to analyse density, elemental site occupation, internal atomic coordinates or the interface to the Al-matrix [2,7]. Additionally, these precipitates are very small and do not produce detectable diffraction peaks. Thus, $\eta'$ is disregarded in the current investigation. $\eta'$-precipitates may transform into the equilibrium phase when they reach a maximum size of 3–4 nm. On the other hand, $\eta$ can form directly on grain boundaries or dislocations [7]. During the reversion treatments at 260 °C, Fig. 2(b), more $\eta$-phase is formed.

### 4.2. Reversion experiments

Fig. 3 shows the results of the SAXS reversion experiments and corresponding modelling results. The evolutions of mean radius and volume fraction over time are plotted for the four different reversion temperatures. Following Deschamps and Perez [16], the reversion process can be divided into three stages:

Stage 1: Dissolution. During heating to temperatures above the solubility line, a rapid decrease in volume fraction is seen. The Gibbs-Thomson effect, governed by interfacial energy and equilibrium solubility, controls the amount of dissolution. Due to the strong increase in the critical radius, all particles shrink and the smallest ones dissolve. As a consequence, the mean radius slightly increases. The model describes the very fast dissolution of precipitates after the increase of the temperature at the two higher temperatures. At the lower temperatures, the fast decrease is not captured by the model.

Stage 2: Growth. In the second stage, the volume fraction reaches a minimum. The solute content in the matrix is increased by dissolution of precipitates. This increase in solute leads to a decrease in the critical radius. When the critical radius drops below the average particle radius, the dissolution of precipitates stops. The remaining precipitates become stable and start to grow. Especially at 290 °C, the experimental data

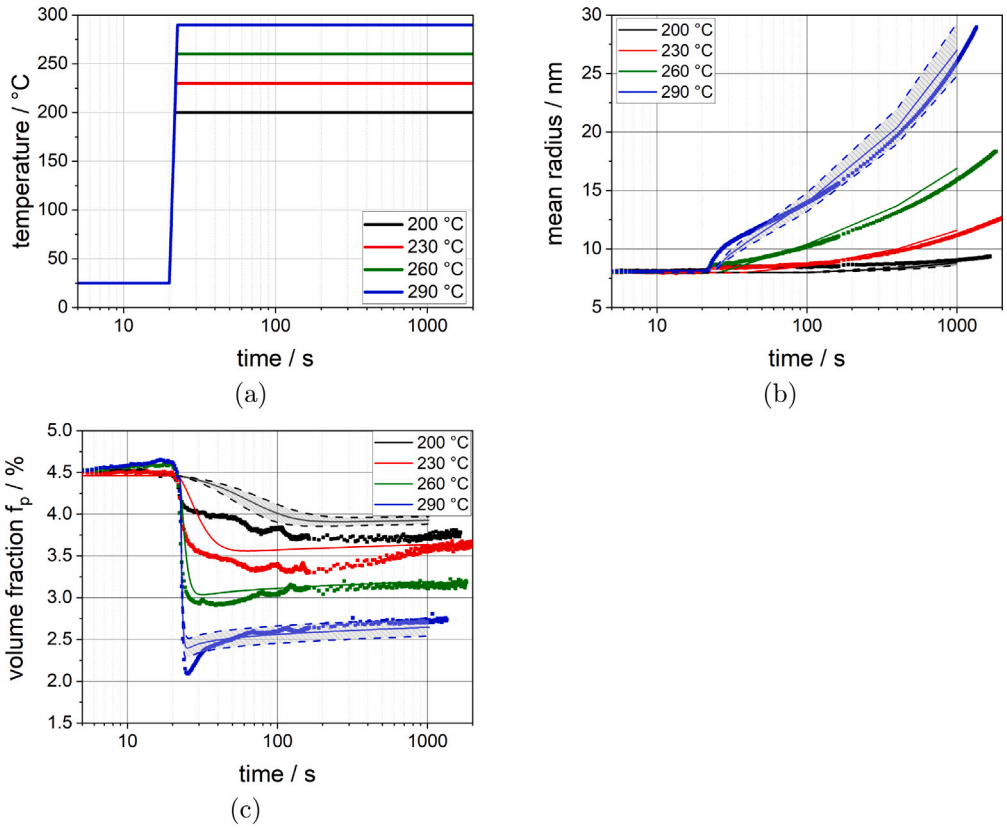


**Fig. 3.** Reversion experiments of AA7050 with simulation results at different temperatures: (a) temperature profile of the reversion experiments, (b) evolution of mean radius, (c) evolution of volume fraction of $\eta$-phase. The square symbols represent the experimental results, while the lines are the modelling results at the respective temperature. The dashed areas around the 200 and 290 °C lines show a temperature variation of ±5 °C in the modelling results to indicate the influence of small temperature changes during reversion experiments.

exhibit a distinct minimum in the volume fraction, which is almost reproduced by the model.

Stage 3: Coarsening. The third stage is dominated by coarsening. The volume fraction increases again due to the growth of precipitates and develops towards the equilibrium volume fraction for the reversion temperature. At higher temperatures, the equilibrium solute content in the matrix increases, leading to lower equilibrium precipitate volume fractions [15]. At this stage the mean radius is rapidly increasing, finally approaching the $t^{1/3}$ growth law, which is reported for coarsening [33]. In the experimental data, this growth law is only observed at 290 °C after 1000 s; at the lower temperatures, the coarsening regime is not reached in the experiment. The simulated final volume fractions are close to the experimental results. At 200 °C the diffusion is slow and the volume fraction has not come close enough to the equilibrium value that the simulation predicts within the observed time interval.

In general, the predictions of the model fit quite well to the experimental reversion data at the investigated temperatures. While the description of the mean radius is very good at all temperatures, the volume fraction is not matched entirely at lower temperatures.

The temperature of the samples in the experiments were continuously measured with thermocouples on the surface. However, slight temperature variations are possible. Therefore, the influence of these variations was modelled and is exemplarily shown here for temperature variations of ±5 °C, at 200 and 290 °C, indicating the significance of small temperature variations during experiments. It can be seen that measurements and modelling at 290 °C agree fully within this range of ±5 °C. The relatively simple reversion experiments show the complexity of precipitation kinetics and illustrate the interplay between temperature, solute content, critical radius and precipitate size distribution. The good description of the experimental reversion results with the present model shows that an appropriate model calibration was achieved.

### 4.3. Modelling of reversion literature data on AA7108

Although a number of reversion experiments for model calibration can be found in literature [15,23], none was found on AA7050. Therefore, the work of Nicolas and Deschamps [15] was used for testing the model predictions on an alloy that is similar to AA7050.

The Al-Zn-Mg alloy AA7108.50 in an overaged T7 state had been used for reversion experiments at 200, 240 and 280 °C, see Fig. 4(a). The alloy composition, the initial size distribution and the heating rate of the present model were adapted to their work, but no other parameters were changed. The alloy was treated as ternary Al alloy with the composition Al-5 Zn-0.8 Mg (in wt.%). The precipitate shape had been assumed as spherical by Nicolas and Deschamps [15]; therefore, spheres were also used in the present model. In general, the model predictions are not as good as for AA7050, see Fig. 4(b), (c), however, the predictions for the mean radius of precipitates at 200 and 240 °C are close to the experimental results; there had been no experimental data for 280 °C . But the agreement is not as good for the volume fraction. Especially the predicted equilibrium volume fraction is significantly smaller than the measured ones. This shows that the used thermodynamic database does not seem to produce correct solubilities for different alloy compositions in the AA7xxx series. The AA7108.50 alloy had a composition of Al-5 Zn-0.8 Mg-0.16 Zr (in wt.%), which differs from the AA7050 composition (Al-6.4 Zn-2 Mg-2.2 Cu (in wt.%)) in a smaller Mg content and the presence of a smaller amount of Zr instead of Cu. These differences are assumed to be the reason for the deviation in the volume fractions. Thus, application of a model that is calibrated for one specific AA7xxx alloy to a different alloy of this series does not seem to be straightforward.

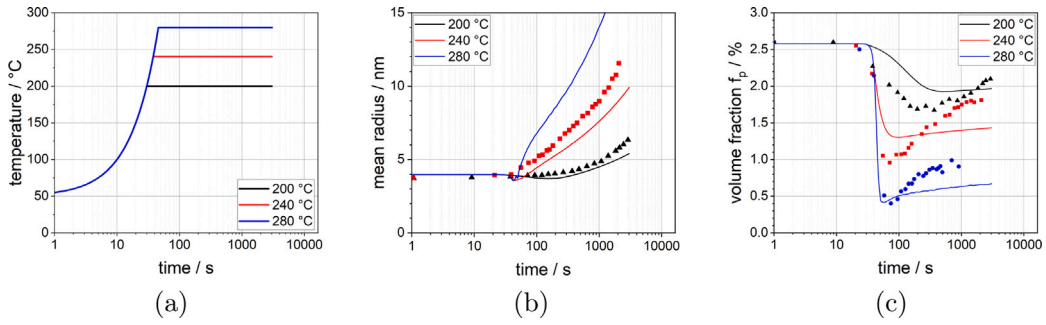


**Fig. 4.** SAXS measurements on AA7108.50 T7 by Nicolas and Deschamps [15] and corresponding modelling results: (a) reversion temperatures, (b) mean radius, (c) volume fraction. The symbols represent the experimental results, while the lines represent the modelling results.

### *4.4. Precipitation kinetics in heat-affected zone during FSW*

The aim of the current work is to predict the influence of heat treatments as they occur in FSW on the precipitation state of A7xxx alloys. The precipitate size distributions in the regions of a friction stir weld that are exposed to elevated temperatures during welding undergo significant changes that influence the mechanical properties and, thus, the performance of the finished product. The knowledge of these changes can eventually be used for predicting mechanical properties after processing. Therefore, the precipitation model used in this work was applied to different time–temperature curves that can be observed in the heat-affected zone during FSW, see Fig. 5(a). The shown time–temperature curves in the HAZ were measured by dos Santos et al. [8] in 3.2 mm thick AA7449 sheets with stationary thermocouples in the material lateral to the tool during FSW with a welding speed of 5 mm/s and a rotational speed of 1300 RPM. The used tool had a diameter of 13 mm. These measured welding temperature cycles were simulated using the dilatometer and in-situ SAXS images were recorded. The measured results are compared with the modelling results.

Similar to reversion, a rapid drop in volume fraction due to the fast increase of the temperature can be seen, Fig. 5(c). The minimum volume fraction correlates with the peak temperature of the welding cycle. Since the small precipitates dissolve first, there is a rapid increase in the mean radius. When the temperature decreases again, precipitates start growing, the volume fraction increases and the mean radius decreases slightly due to the faster growth of small precipitates. When the temperature drops below 120 °C, there are only very small changes until room temperature is reached. In general, there is an excellent agreement between numerical and experimental results. The final volume fractions match well and the difference in mean radius is less than 0.7 nm.

The high peak temperatures in the heat-affected zone lead to the growth or even dissolution of precipitates. Since these precipitates are responsible for the mechanical properties of AA7050, i.e. the hardness, the dissolution and growth leads to a reduction in hardness in the heat-affected zone. This has been extensively described in the literature on FSW, see e.g. [34,35].

These results can be directly compared to results obtained by Kamp et al. [17] who developed a Kampmann-Wagner model that can describe both metastable $\eta'$- and equilibrium $\eta$-precipitates in AA7449. Their model also predicted the precipitation kinetics during temperature curves in heat-affected zones occuring in FSW with a maximum temperature of 330 °C. For AA7449 in the T7 condition, only $\eta$-precipitates with a composition of $MgZn_2$ were used in the starting size distribution. The model predicted dissolution and coarsening of the $\eta$-phase, similar to the results in this work.

The welding examples demonstrate that it is possible to model precipitation kinetics in AA7050 during temperature cycles as they occur in FSW processes. The large variation of the maximum temperature requires thermodynamic databases that cover these temperature ranges correctly. Based on the good agreement between experimental and modelling results, reasonable predictions for the modelling of other time–temperature curves are expected as well.

### *4.5. Influence of welding speed on precipitation kinetics*

The model gives a reasonable description of the precipitation kinetics that occur in the heat-affected zone during FSW with a welding speed of 5 mm/s. It was shown in the previous section that precipitation kinetics in a temperature range of 200–340 °C are well described and hence, the model can be used to predict precipitation kinetics under the influence of arbitrary temperature cycles. Thus, we can use the model for studying the influence of different welding speeds on the precipitate distribution in the AA7050-T7451 alloy. For that purpose, a set of welding temperature cycles is calculated based on the master curve measured at a welding speed of 5 mm/s. For simplicity, faster welding speeds are mimicked by multiplying the time scale of the welding time temperature curves in Fig. 5(a), using factors of 0.125, 0.25 and 0.5. Slower welding speeds are mimicked by multiplying it with the factors 2 and 4. With this approach, welding speeds in the range of 0.6–20 mm/s are roughly described. Different maximum temperatures represent certain distances from the weld line.

The employed time–temperature curves for a temperature maximum of 340 °C are shown in Fig. 6(a). The model predictions show that slower welding speeds lead to a much stronger coarsening of the precipitates. While the radius stays constant at 8 nm at a welding speed of 20 mm/s, the precipitates grow to a radius of 21 nm at a welding speed of 0.6 mm/s, Fig. 6(b). The influence of welding speed on the final volume fraction is less pronounced, Fig. 6(c).

The minimum in volume fraction is nearly identical for all welding speeds because it depends only on the solubility as a function of temperature. Thus, diffusion in this alloy is fast enough for the volume fraction to follow the changes in temperature. The final volume fraction is increasing with decreasing welding speeds. Different heating rates as well as cooling rates occur for different welding speeds. At the high welding speed of 20 mm/s, the heating rate is so high so that there is not enough time for significant growth of precipitates. In contrast, at low welding speeds, there is more time for diffusion and precipitates can grow, increasing the final volume fraction.

As mentioned above, a series of calculations were carried out for different welding speeds in the range of 0.6–20 mm/s and different maximum temperatures in the range of 200–340 °C. The results of these calculations in Fig. 7 show that strong coarsening of precipitates can only be expected at high peak temperatures, where diffusion is fast, and slow welding speeds that give sufficient time for precipitate growth, i.e. in the upper left corner in Fig. 7(a). Up to peak temperatures of 250 °C, no significant coarsening is seen. At the highest welding speed, no coarsening occurs even at the highest maximum temperature of 340 °C.

At low welding speeds, the final volume fraction remains high, even at high peak temperatures, see Fig. 7(b). Above 250 °C, the final volume fraction decreases with increasing welding speed. Below 250 °C, this trend is changed and the final volume fraction increases with increasing welding speeds. At high welding speeds and low maximum temperatures there is hardly a change compared to the initial precipitate size distribution.

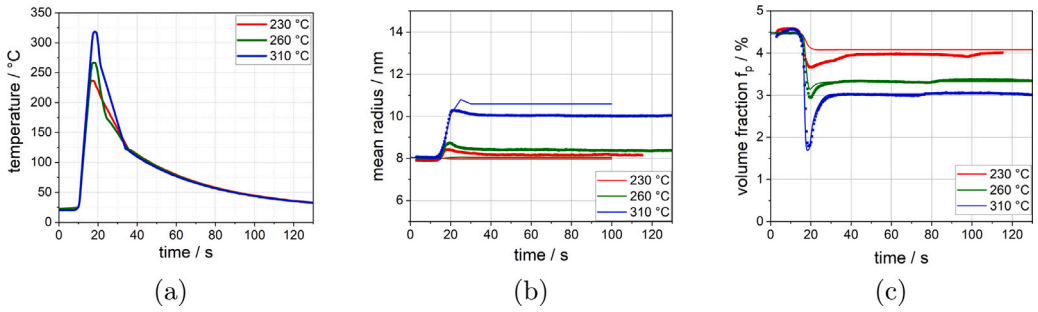


**Fig. 5.** Experimental and modelling results of FSW welding simulations: (a) time–temperature profiles representative for HAZ during FSW process at different maximum process temperatures, (b) evolution of mean radius, (c) evolution of volume fraction. The square symbols represent the experimental results at 230, 260 and 310 °C. The continuous lines illustrate the modelling results at the respective temperature.

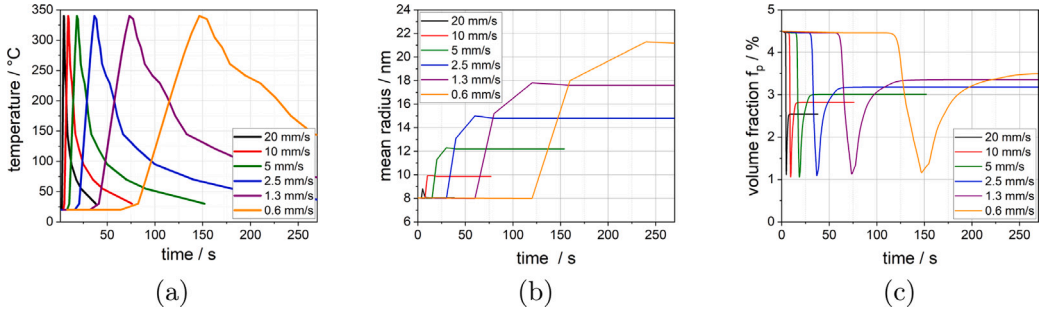


**Fig. 6.** Modelling the influence of different welding speeds on precipitation: (a) time–temperature curves with a maximum temperature of 340 °C, (b) evolution of mean radius, (c) evolution of volume fraction.

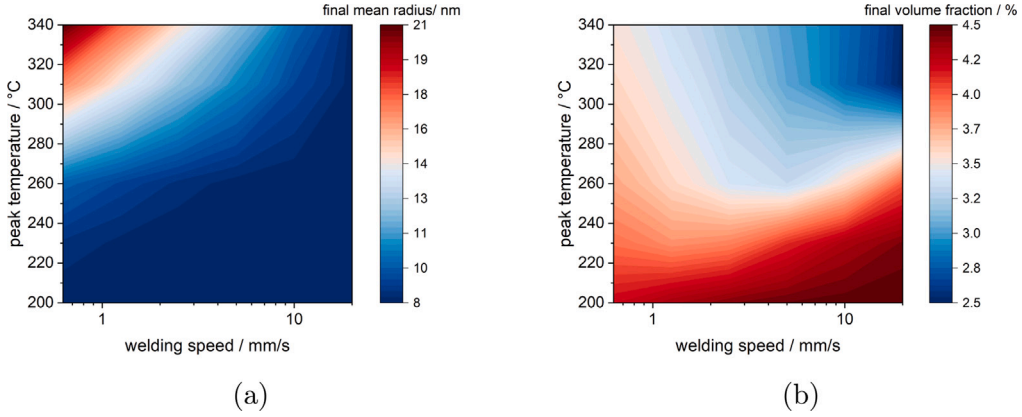


**Fig. 7.** Modelling the influence of maximum temperature and welding speed on $\eta$-precipitates in AA7050: (a) final mean radius, (b) final volume fraction.

In conclusion, one can derive the following statements for the FSW process in AA7050 alloys: (i) Welding speeds below 3 mm/s can lead to serious precipitate coarsening at locations where the maximum temperature is above 300 °C. (ii) In regions with peak temperatures below 250 °C, the precipitate volume fraction stays high and significant softening does not take place at the investigated welding speeds. Hence, this model can help to provide guidelines for suitable welding parameters in AA7050.

## 5. Summary

The non-equilibrium precipitation kinetics, as they occur during solid-state welding processes, were analysed in an AA7050 aerospace Al alloy using in-situ small-angle X-ray scattering (SAXS) at a high-energy synchrotron beamline and numerical modelling using the commercial software package Pandat. Calibration of model parameters was done using in-situ reversion and welding heat cycle experiments. In addition, the capability of the model to describe other alloys of the AA7xxx series with slightly different chemical composition was tested with literature data. As a result, the model was found to describe the studied precipitation kinetics with good accuracy.

In a second step, the model was used for predicting precipitation kinetics for a two-dimensional parameter variation, covering different welding speeds and maximum temperatures. The maximum temperature reflects different distances from the weld line. From the model predictions, the influence of the welding parameters on the final precipitation state could be derived and can act as recommendations for process parameters for friction stir welding of AA7050.

The current work has shown how commercial software such as Pandat can be used to predict precipitate size distributions as a function of thermal history. The results are expected to be reliable for AA7050 alloy, however, working with other alloys of the AA7xxx series requires further studies on the influence of elements other than Mg and Zn (mostly Cu) on the precipitation kinetics. Moreover, databases

are needed that properly cover the corresponding thermodynamics. Additionally, further knowledge on the composition of precipitates and matrix is needed. e.g. from atom probe analyses. The present results are the basis for future studies on the mechanical properties of friction stir welds in AA7xxx alloys.

## CRediT authorship contribution statement

**Susanne Henninger:** Writing – original draft, Investigation, Formal analysis. **Rupesh Chafle:** Writing – original draft, Software, Investigation. **Emad Maawad:** Methodology, Investigation. **Benjamin Klusemann:** Writing – review & editing, Supervision, Project administration, Funding acquisition. **Martin Müller:** Writing – review & editing, Supervision. **Peter Staron:** Writing – review & editing, Writing – original draft, Supervision, Project administration.

## Declaration of competing interest

The authors declare that they have no known competing financial interests or personal relationships that could have appeared to influence the work reported in this paper.

## Acknowledgements

We acknowledge DESY (Hamburg, Germany), a member of the Helmholtz Association HGF, for the provision of experimental facilities. Parts of this research were carried out at PETRA III at the High Energy Materials Science beamline P07. Open Access funding enabled and organized by Projekt DEAL. Rupesh Chafle and Benjamin Klusemann acknowledge funding from the European Research Council (ERC) under the European Union's Horizon 2020 research and innovation program (grant agreement No 101001567).

## Data availability

The obtained data of this research is online available at Zenodo (https://doi.org/10.5281/zenodo.14749904).

## References

[1] X.-M. Li, M. Starink, Effect of compositional variations on characteristics of coarse intermetallic particles in overaged 7000 aluminium alloys, Mater. Sci. Technol. 17 (11) (2001) 1324–1328.
[2] F. Cao, J. Zheng, Y. Jiang, B. Chen, Y. Wang, T. Hu, Experimental and DFT characterization of $\eta'$ nano-phase and its interfaces in Al-Zn-Mg-Cu alloys, Acta Mater. 164 (2019) 207–219.
[3] M. Ahmed, M. El-Sayed Seleman, D. Fydrych, G. Çam, Friction stir welding of aluminum in the aerospace industry: The current progress and state-of-the art review, Materials 16 (8) (2023) 2971.
[4] L. Berg, J. Gjønnes, V. Hansen, X. Li, M. Knutson-Wedel, G. Waterloo, D. Schryvers, L. Wallenberg, GP-zones in Al-Zn-Mg alloys and their role in artifical aging, Acta Mater. 49 (17) (2001) 3443–3451.
[5] J. Lendvai, Precipitation and strengthening in aluminium alloys, Mater. Sci. Forum 217–222 (1996) 43–56.
[6] M. Styles, T. Bastow, M. Gibson, C. Hutchinson, Substitution of Cu and/or Al in $\eta$ phase ($MgZn_2$) and the implications for precipitation in Al-Zn-Mg-(Cu) alloys, Intermetallics 49 (2014) 40–51.
[7] A. Kverneland, V. Hansen, G. Thorkildsen, H. Larsen, P. Pattison, X. Li, J. Gjønnes, Transformations and structures in the Al-Zn-Mg alloy system: A diffraction study using synchrotron radiation and electron precession, Mater. Sci. Eng. A 528 (3) (2011) 880–887.
[8] J. dos Santos, P. Staron, T. Fischer, J. Robson, A. Kostka, P. Colegrove, H. Wang, J. Hilgert, L. Bergmann, L. Hütsch, N. Huber, A. Schreyer, Understanding precipitate evolution during friction stir welding of Al-Zn-Mg-Cu alloy through in-situ measurement coupled with simulation, Acta Mater. 148 (2018) 163–172.
[9] A. Stark, M. Oehring, F. Pyczak, A. Schreyer, In situ observation of various phase transformation paths in Nb-rich TiAl alloys during quenching with different rates, Adv. Eng. Mater. 13 (8) (2011) 700–704.
[10] CompuTherm LLC, Introducing Pandat software - an integrated modeling platform for materials design, 2024, https://computherm.com/. (Accessed 28 January 2025).
[11] Thermo-Calc Software, Thermo-calc software: Computational materials engineering, 2024, https://thermocalc.com/. (Accessed 28 January 2025).
[12] W. Cao, S.-L. Chen, F. Zhang, K. Wu, Y. Yang, Y. Chang, R. Schmid-Fetzer, W. Oates, PANDAT software with PanEngine, PanOptimizer and PanPrecipitation for multi-component phase diagram calculation and materials property simulation, Calphad 33 (2009) 328–342.
[13] W. Cao, F. Zhang, S. Chen, C. Zhang, Y. Chang, An integrated computational tool for precipitation simulation, JOM 63 (7) (2011) 29–34.
[14] R. Kampmann, R. Wagner, Kinetics of precipitation in metastable binary alloys - theory and application to Cu-1.9at.% Ti and Ni-14at.% Al, Decompos. Alloys: Early Stages Pergamon Press Oxf. (1984) 91–103.
[15] M. Nicolas, A. Deschamps, Characterisation and modelling of precipitate evolution in an Al-Zn-Mg alloy during non-isothermal heat treatments, Acta Mater. 51 (2003) 6077–6094.
[16] A. Deschamps, M. Perez, Mesoscopic modelling of precipitation: A tool for extracting physical parameters of phase transformations in metallic alloys, C. R. Phys. 11 (3) (2010) 236–244.
[17] N. Kamp, A. Sullivan, R. Tomasi, J. Robson, Modelling of heterogeneous precipitate distribution evolution during friction stir welding process, Acta Mater. 54 (8) (2006) 2003–2014.
[18] N. Schell, R. Martins, F. Beckmann, H. Ruhnau, R. Kiehn, A. Schreyer, The high energy materials science beamline at PETRA III, Mater. Sci. Forum 571–572 (2008) 261–266.
[19] J. Ilavsky, Nika: software for two-dimensional data reduction, J. Appl. Crystallogr. 45 (2) (2012) 324–328.
[20] J. Ilavsky, P. Jemian, Irena: tool suite for modeling and analysis of small-angle scattering, J. Appl. Crystallogr. 42 (2) (2009) 347–353.
[21] P. Villars, $MgZn_2$ crystal structure (sd_0261233), pauling file in: inorganic solid phases, SpringerMaterials (online database), Springer (2023).
[22] C. Liu, A. Davis, J. Fellowes, P. Prangnell, D. Raabe, P. Shanthraj, CALPHAD-informed phase-field model for two-sublattice phases based on chemical potentials: $\eta$-phase precipitation in Al-Zn-Mg-Cu alloys, Acta Mater. 226 (2022) 117602.
[23] T. Marlaud, A. Deschamps, F. Bley, W. Lefebvre, B. Baroux, Evolution of precipitate microstructures during the retrogression and re-aging heat treatment of an Al-Zn-Mg-Cu alloy, Acta Mater. 58 (14) (2010) 4814–4826.
[24] C. Kammerer, S. Behdad, L. Zhou, F. Betancor, M. Gonzalez, B. Boesl, Y. Sohn, Diffusion kinetics, mechanical properties, and crystallographic characterization of intermetallic compounds in the Mg-Zn binary system, Intermetallics 67 (2015) 145–155.
[25] CompuTherm LLC, PANDAT$^{TM}$ 2021 user's guide, 2021.
[26] The Materials Project, Data for $MgZn_2$ (mp-1124) from database version v2023.11.1, 2023.
[27] A. Jain, S. Ong, G. Hautier, W. Chen, W. Richards, S. Dacek, S. Cholia, D. Gunter, D. Skinner, G. Ceder, K. Persson, Commentary: The materials project: A materials genome approach to accelerating materials innovation, APL Mater. 1 (2013) 011002.
[28] W. Kraus, G. Nolze, POWDER CELL - a program for the representation and manipulation of crystal structures and calculation of the resulting X-ray powder patterns, J. Appl. Crystallogr. 29 (1996) 301–303.
[29] J. Friauf, The crystal structure of magnesium di-zincide, Phys. Rev. 29 (1) (1927) 34–40.
[30] M. Bown, P. Brown, The structure of $FeCu_2Al_7$ and T(CoCuAl), Acta Crystallogr. 9 (1956) 911–914.
[31] The Materials Project, Data for $Al_7Cu_2Fe$ (mp-4689) from database version v2023.11.1, 2023.
[32] J. Robson, P. Prangnell, Dispersoid precipitation and process modelling in zirconium containing commercial aluminium alloys, Acta Mater. 49 (4) (2001) 599–613.
[33] F. Fischer, J. Svoboda, P. Fratzl, A thermodynamic approach to grain growth and coarsening, Philos. Mag. 83 (9) (2003) 1075–1093.
[34] R. Mishra, Z. Ma, Friction stir welding and processing, Mater. Sci. Eng. R 50 (1) (2005) 1–78.
[35] M. Ahmed, S. Ataya, M. El-Sayed Seleman, H. Ammar, E. Ahmed, Friction stir welding of similar and dissimilar AA7075 and AA5086, J. Mater. Process. Technol. 242 (2017) 77–91.